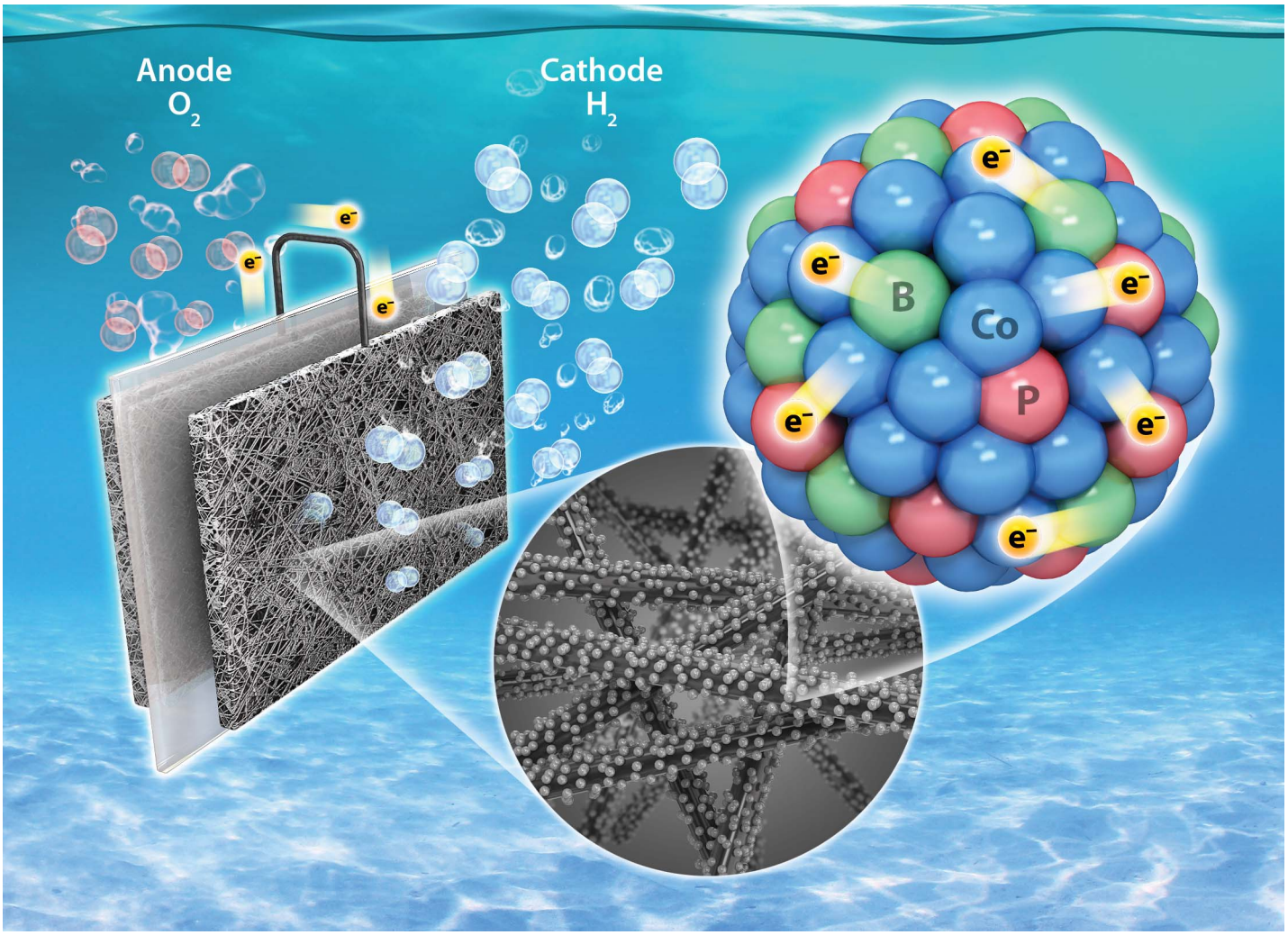
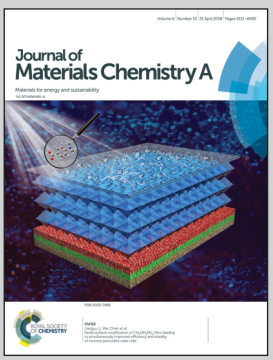


Showcasing a study on the synergetic effect of electron transfer in a Co-P-B catalyst for the hydrogen evolution reaction by Prof. Soo-Kil Kim and Prof. Sang Hyun Ahn at Chung-Ang University, Republic of Korea.

Electrodeposited amorphous Co–P–B ternary catalyst for hydrogen evolution reaction

The facile fabrication of a porous gas diffusion electrode employing amorphous Co-P-B ternary catalysts and the synergetic effect of electron transfer among three elements on high catalytic activity for the hydrogen evolution reaction are demonstrated.

As featured in:



See Soo-Kil Kim, Sang Hyun Ahn *et al.*, *J. Mater. Chem. A*, 2018, **6**, 6282.

ROYAL SOCIETY OF CHEMISTRY

rsc.li/materials-a

Registered charity number: 207890

Journal of Materials Chemistry A

PAPER

View Article Online
View Journal | View Issue

Check for updates

Cite this: J. Mater. Chem. A, 2018, 6, 6282

Electrodeposited amorphous Co–P–B ternary catalyst for hydrogen evolution reaction†

Junhyeong Kim,[a] Hyunki Kim,[a] Soo-Kil Kim*[b] and Sang Hyun Ahn*[a]

Received 17th December 2017
Accepted 18th February 2018

DOI: 10.1039/c7ta11033b

rsc.li/materials-a

The catalytic activity of amorphous Co–P–B catalysts electrodeposited on carbon paper (CP) for the hydrogen evolution reaction (HER) was investigated in aqueous 0.5 M H_2SO_4 electrolyte. Based on the measured double layer capacitance (C_{dl}) and HER activity, it was found that the HER intrinsic activity exhibited volcano behavior when plotted as a function of the B/P ratio in the Co–P–B catalyst. It was revealed that based on the electronic structures of the elements, electron transfer among the three elements is a significant factor for enhancing the intrinsic activity for the HER. The highest activity was obtained with a B/P ratio of ~1, where electron transfer among the three elements was maximized.

Published on 21 February 2018. Downloaded by Chungang University on 4/17/2019 9:25:29 AM.

Introduction

Due to the global warming, numerous studies have been conducted on the development of eco-friendly hydrogen energy.[1] Among the various methods of hydrogen production,[2–5] the electrolysis of water has been recognized as promising owing to the simplicity of the system, moderate operating conditions, unlimited raw material, and high purity of the hydrogen generated.[6] Moreover, if the water electrolysis system is driven by electricity from renewable energy such as sunlight or wind power, a completely eco-friendly system can be constructed.[7] In order to overcome the disadvantages of conventional water electrolyzers (*e.g.*, ohmic loss),[8] membrane electrode assembly (MEA)-based electrolyzers have been investigated, including proton exchange membrane water electrolyzers (PEMWEs)[9] and anion exchange membrane water electrolyzers (AEMWEs).[10] It is known that the PEMWE is advantageous over the AEMWE owing to the higher hydrogen production rate and energy efficiency.[11] However, commercialization of the PEMWE is limited as this system is not cost-effective due to the extensive use of noble metal-based catalysts. Platinum (Pt) is recognized as the best catalyst for the cathode for the HER, but is very expensive. Consequently, it is essential to develop HER catalysts that are cost effective and exhibit high activity.

Unlike oxygen evolution reaction (OER) catalysts for the anode, transition metal-based catalysts (*e.g.*, metal alloys,[12–14] phosphides,[15–19] sulfides,[20–22] borides,[23–25] nitrides,[26–28] and carbides-[29,30]) can be used for the HER in acidic solution because they are electrochemically stable in the operating potential window of the HER.[31] Cobalt phosphides exhibit excellent HER activity and stability, and therefore, extensive studies on their morphological[32] and compositional control have been undertaken.[33] In terms of morphological control, various structures of cobalt phosphides with increased active sites (as well as certain facets) have been reported, such as spheres,[34,35] nanoneedles,[36] nanorods,[37] nanoparticles,[38] nanowires,[39,40] nanosheets,[41] polyhedrons,[42,43] films,[44] and foams.[45] Moreover, many studies have explored the relationship between the HER performance and composition of cobalt phosphide.[18] Callejas and colleagues suggested that the HER overpotential of CoP was lower than that of Co_2P with a homogeneous morphology.[18] It has been reported that the catalytic performance of cobalt phosphide for the HER increased with an increase in the P ratio,[46] which is similar to the behaviour observed for nickel phosphide[16] and molybdenum phosphide.[19] This enhancement may be derived because electron-rich and highly electronegative phosphorus acts as an effective active site for the HER by altering the hydrogen binding energy.[47] Transition metal borides have been investigated by similar approaches.[25,48–51] Unlike the case of cobalt phosphide, it was revealed that the crystallinity of cobalt boride affected the direction of electron transfer between cobalt and boron.[49] In the case of amorphous Co–B, the electrons localized on boron were transferred to fill the vacant d-orbital of cobalt; thus, electron-rich cobalt acted as an active site for the HER in $NaBH_4$ solution. Further improvement of the HER performance has been achieved with Co–Ni–B under various pH conditions.[50]

Considering the advantages of cobalt phosphides and borides, cobalt-based complexes containing phosphorus and boron (Co–P–B) may be promising catalysts for the HER,[51] however the researches about this are rare. Co–P–B species are generally synthesized by chemical reduction using $NaBH_4$ (ref. 52) where $NaBH_4$ serves as a strong reducing agent as well as a boron source in the aqueous solution. However, this method

[a]School of Chemical Engineering and Material Science, Chung-Ang University, 84 Heukseokno, Dongjak-gu, Seoul, 06974, Republic of Korea. E-mail: shahn@cau.ac.kr
[b]School of Integrative Engineering, Chung-Ang University, 84 Heukseokno, Dongjak-gu, Seoul, 06974, Republic of Korea. E-mail: sookilkim@cau.ac.kr

† Electronic supplementary information (ESI) available. See DOI: 10.1039/c7ta11033b

This journal is © The Royal Society of Chemistry 2018

Published on 21 February 2018. Downloaded by Chungang University on 4/17/2019 9:25:29 AM.

has demerits in that the process takes a long time and requires a relatively high temperature (~70 °C). On the other hand, the electrodeposition method facilitates a simple and short process at room temperature under ambient pressure.[53,54] It is also known to be advantageous in offering easy control of the morphology and composition by adjustment of the process parameters, such as the electrolyte composition, deposition potential, and time. The methodological simplicity enables a quick survey of the relationship between the material properties and catalytic activity. Furthermore, with respect to the fabrication of gas diffusion electrodes (GDEs), the electrodeposition method provides a one-pot process that is advantageous over the conventional GDE fabrication process consisting of catalyst synthesis and following coating process.[55]

The results presented herein demonstrate the direct electrodeposition of Co–P–B catalysts on carbon paper (CP) as a GDE for the PEMWE. Controlling the precursor concentration in the electrodeposition bath enables easy control of the catalyst composition, especially in B/P ratio. The HER activity of the catalyst is investigated in acidic environment. Based on the electrochemical surface area (ECSA), the HER intrinsic activity shows volcano behaviour as a function of the B/P ratio in the catalysts. Analysis of the electronic structure reveals that electron transfer among the three elements is significantly affected by the B/P ratio.

Experimental

Electrodeposition of cobalt–phosphorus–boron (Co–P–B)

As a working electrode, the CP substrate was pre-treated by immersion in 30% HNO_3 at 50 °C for 30 min in order to provide hydrophilicity to the surface.[56] A lab-made Teflon cell with an area of 1.13 cm^2 exposed to the deposition electrolyte was used as the three-electrode cell system for electrodeposition. A Pt wire and a saturated calomel electrode (SCE, KCl saturated) were used as the counter and reference electrodes, respectively. The composition of the electrolyte used for electrodeposition is as follows: the concentration of $CoCl_2 \cdot 6H_2O$ (99.0%, DAEJUNG), as a cobalt precursor, was fixed at 1 mM with a 0.1 M NaCl (50%, Fluka) supporting electrolyte. $NaH_2PO_2 \cdot H_2O$ (95.0%, YAKURI) and H_3BO_3 (99.5%, DAEJUNG) were added as a phosphorus and boron source, respectively, maintaining a total concentration of 0.5 M.[57] The electrolytes were purged by bubbling with N_2 gas for 30 min to remove dissolved oxygen in the electrolyte. Electrodeposition was performed by applying a constant deposition potential of −1.5 V_{SCE} for 600 s, where the potential was controlled by a potentiostat (Autolab PGSTAT302N, Metrohm) at room temperature and atmospheric pressure.

Characterization

Field-emission scanning electron microscopy (FESEM, SIGMA, Carl Zeiss) and X-ray diffraction (XRD, New D8-Advance, BRUKER) were used to examine the surface morphology and crystal structure of the Co–P–B catalyst, respectively. X-ray photoelectron spectroscopy (XPS, K-alpha+, ThermoFisher Scientific) was used to investigate the electronic structure and compositional ratio of the elements at the catalyst surface. Transmission electron microscopy (TEM, JEOL Ltd., JEM-2100F) with scanning transmission electron microscopy (STEM, Bright-field, lattice resolution: 0.2 nm) was employed to analyze the shape and composition of a single Co–P–B catalyst particle. The crystal structure was confirmed from the selected area electron diffraction (SAED) pattern.

Electrochemical measurements

Electrochemical analysis was performed by using a three-electrode system connected to a potentiostat (Autolab PGSTAT302N, Metrohm). The working electrode was Co–P–B electrodeposited on CP, and a Pt wire and a SCE were used as the counter and reference electrode, respectively. In order to investigate the surface roughness of electrodeposited Co–P–B, cyclic voltammetry (CV) was conducted in the non-faradaic potential range in 0.5 M H_2SO_4 (95.0%, JUNSEI). The C_{dl} was determined by plotting the mean value of the anodic and cathodic currents as a function of the scan rate. The HER activity tests were performed in 0.5 M H_2SO_4 (95.0%, JUNSEI) by CV scans in the potential range of −0.2 V_{SCE} to −0.8 V_{SCE} at a scan rate of 50 mV s^{-1}. All potentials were converted relative to the reversible hydrogen electrode (RHE). Before all electrochemical measurements, the electrolyte was purged by bubbling with N_2 gas for 30 min.

Results and discussion

Electrodeposition was conducted on pre-treated CP (Fig. 1a) by varying the electrolyte composition at a constant potential of −1.5 V_{SCE} for 600 s. The composition of the electrolytes used for

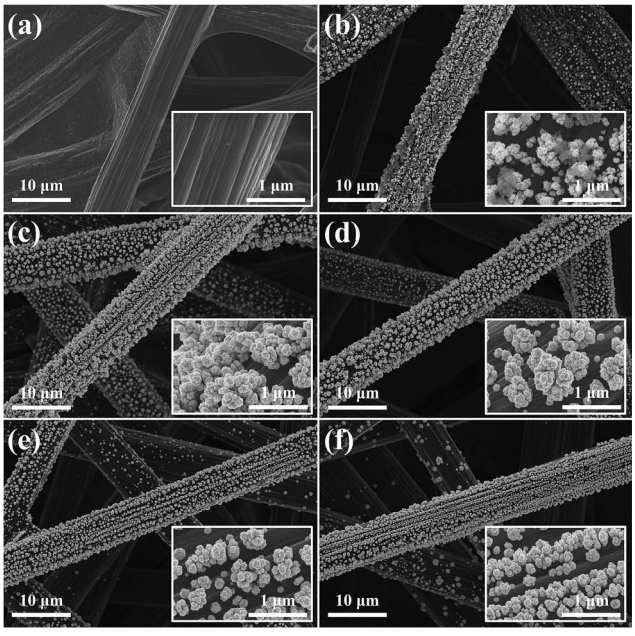


Fig. 1 Low- and (inset) high-magnification FESEM images of (a) CP and (b–f) electrodeposited Co–P–B catalysts on CP using each electrolyte composition: (b) $Co_{57}P_{27}B_{16}$/CP, (c) $Co_{53}P_{27}B_{20}$/CP, (d) $Co_{59}P_{20}B_{21}$/CP, (e) $Co_{41}P_{21}B_{38}$/CP, (f) $Co_{34}P_{20}B_{46}$/CP.

Published on 21 February 2018. Downloaded by Chungang University on 4/17/2019 9:25:29 AM.

electrodeposition are summarized in Table S1 (ESI†) For all of the Co–P–B catalysts (Fig. 1b–f), the lower magnification FESEM images show that the distribution of the deposits on the surface of the CP was mostly uniform, indicating that pretreatment of CP conferred hydrophilicity to the surface for electrodeposition.[56] The negligible difference in the cluster size means that the morphology of the Co–P–B catalysts was not significantly affected by the electrolyte composition. The nomenclature of the catalysts reflects their composition measured by XPS analysis (see Table S1, ESI†). With an increase in the B/P precursor ratio in the electrolyte, the B/P atomic ratio of the Co–P–B catalysts increase, as shown in Fig. S1 (ESI†). As a reference, the electrodeposition was carried out without adding B or P sources to the electrolyte, resulting in a different morphology than that of the Co–P–B catalysts (Fig. S2a and b, ESI†). Fig. 2 shows the XRD patterns of the CP before and after electrodeposition of the Co–P–B catalysts. Three peaks were observed at 40.6°, 43.2° and 54.7° in the profile of the CP substrate.

Fig. 3a shows the TEM image of a single $Co_{59}P_{20}B_{21}$/CP particle which exhibited the highest HER performance. The size of the individual particles is in a range of 100–200 nm, which corresponds well with the FESEM analysis (see inset of Fig. 1d). From the SAED pattern (Fig. 3b), it is confirmed that there is no diffraction ring, indicating the amorphous structure of the $Co_{59}P_{20}B_{21}$/CP catalyst, which is consistent with the XRD pattern (Fig. 2). As shown in the elemental map (Fig. 3c–e), cobalt and phosphorus are uniformly distributed in the single $Co_{59}P_{20}B_{21}$/CP particle. In the case of boron, the mapping image was not trustworthy due to the lower intensity of the signal because boron is a light element.

The catalytic activity of the electrodeposited Co–P–B catalyst for the HER was tested by CV scanning in N_2-purged 0.5 M H_2SO_4 solution. Fig. 4a shows the forward CV scans where compensation was made for the electrolyte resistance. The HER activity of the CP substrate was negligible. For the Co–P–B catalysts, the HER activity followed the order: $Co_{59}P_{20}B_{21}$/CP > $Co_{41}P_{21}B_{38}$/CP > $Co_{34}P_{20}B_{46}$/CP ≈ $Co_{53}P_{27}B_{20}$/CP > $Co_{57}P_{27}B_{16}$/CP. Fig. 4b shows the Tafel plot with a slope in the range of about 62–68 mV dec^{-1}, indicating that in the presence of the Co–P–B catalysts, the HER followed the Volmer–Heyrovsky mechanism (Volmer reaction: $M + H^+ + e^- \rightarrow M - H_{ad}$, Heyrovsky reaction: $M - H_{ad} + M - H_{ad} \rightarrow 2M + H_2$).[58] The exchange current density for the HER is calculated and the highest value was 0.031 mA cm^{-2} for $Co_{59}P_{20}B_{21}$/CP, as summarized in Table S2 (ESI†). The C_{dl} was determined by CV at scan rates of 10–200 mV s^{-1} in the non-faradaic potential range of each catalyst (Fig. S3, ESI†). The mean value of the anodic and cathodic current density is plotted as a function of the scan rate (Fig. 4c). The slope shows the C_{dl} representing the surface roughness of

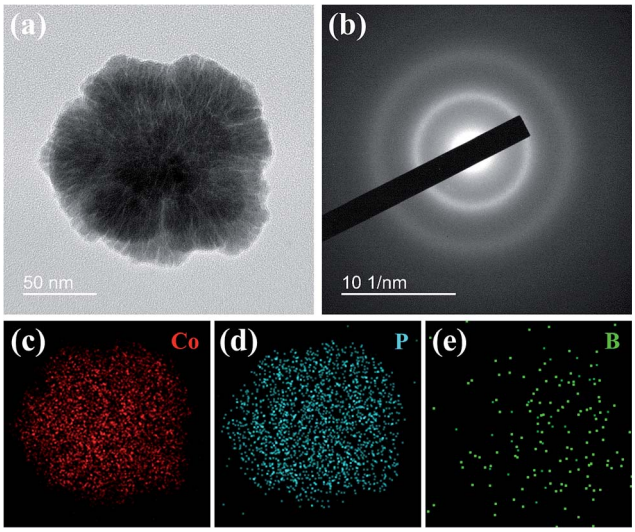


Fig. 3 (a) TEM image and (b) SAED patterns of $Co_{59}P_{20}B_{21}$/CP catalyst. STEM and elemental mapping images of $Co_{59}P_{20}B_{21}$/CP catalyst: (c) cobalt, (d) phosphorus, (e) boron.

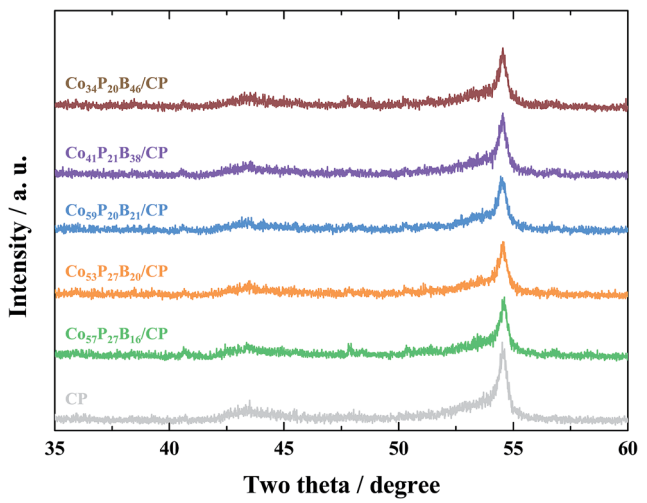


Fig. 2 XRD patterns of CP and electrodeposited Co–P–B catalysts on CP with each atomic composition.

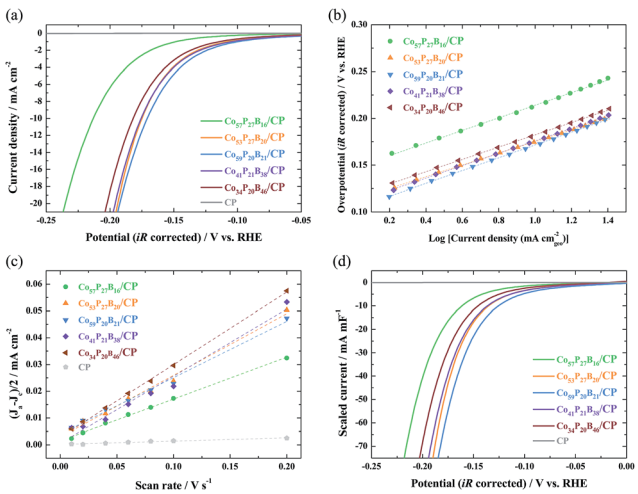


Fig. 4 (a) Polarization curves of Co–P–B catalysts at a scan rate of 50 mV s^{-1}. (b) Tafel plots of Co–P–B catalysts. (c) Double layer capacitance for Co–P–B catalysts as a function of scan rate. (d) Polarization curves of Co–P–B catalysts based on scaled current for HER intrinsic activity. All the electrochemical measurements were performed in 0.5 M H_2SO_4.

This journal is © The Royal Society of Chemistry 2018

Published on 21 February 2018. Downloaded by Chungang University on 4/17/2019 9:25:29 AM.

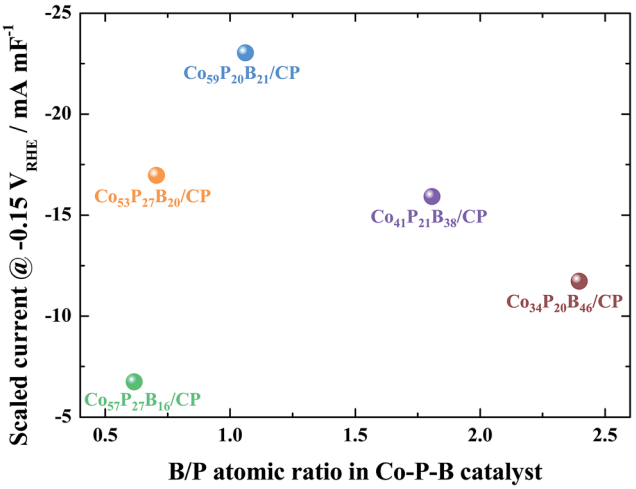


Fig. 5 Volcano plots of scaled current according to B/P atomic ratio in Co–P–B catalysts.

Co–P–B catalysts. In order to evaluate the intrinsic activity, the forward CV scans for the HER is normalized by the measured C_{dl} (Fig. 4d) excluding the effect of the ECSA. The scaled current representing the intrinsic HER activity follows the order: $Co_{59}P_{20}B_{21}$/CP > $Co_{53}P_{27}B_{20}$/CP > $Co_{41}P_{21}B_{38}$/CP > $Co_{34}P_{20}B_{46}$/CP > $Co_{57}P_{27}B_{16}$/CP. In general, the intrinsic activity of a catalyst for the HER is significantly affected by changes in the binding energy of hydrogen caused by specific crystal facets and the elemental composition.[18] For the prepared Co–P–B catalysts, the intrinsic activity originating from the facets could be excluded in the present study as no facets were present based on the absence of defined peaks in the XRD pattern (Fig. 2) and of a diffraction ring in the SAED pattern (Fig. 3b).

Fig. 5 demonstrates the HER scaled current at −0.15 V_{RHE} from Fig. 4d as a function of the B/P ratio in the Co–P–B catalysts. Below the B/P ratio of ~1, the scaled current was increased by increase of the B/P ratio. The highest intrinsic HER activity was observed for $Co_{59}P_{20}B_{21}$/CP having a B/P ratio of ~1 and then, the scaled current was decreased by further increase of the B/P ratio. The volcano relationship between the scaled the current and B/P ratio indicates the existence of a significant interrelation among the three elements, conceivably affecting the hydrogen binding energy on the surface of Co–P–B/CP catalysts.

To evaluate the effect of the elements on the HER intrinsic activity, XPS analysis was conducted for each of the Co–P–B catalysts on CP (Fig. 6). The XPS spectra of all the Co–P–B catalysts show two peaks of the Co $2p_{3/2}$ state around 778.6 eV and 781.5 eV (Fig. 6a). The measured binding energy of 778.6 eV is positively shifted relative to the reported binding energy of metallic Co (778.1 eV),[36] indicating that Co on the catalyst surface is oxidized due to the formation of native oxide or electron depletion by neighbouring P or B elements. In addition, the peak ratio of metallic and oxidized Co changed depending on the B/P ratio in the catalysts. Fig. 6b shows the P 2p XPS spectra of the Co–P–B catalysts. The two separated peaks in the range of 128.0–131.5 eV represent the P $2p_{3/2}$ and $2p_{1/2}$ states, whereas the peak at higher binding energy corresponds to the oxidized state of phosphorus. Compared with the reported binding energy of elemental P (130.1 eV),[59] the P $2p_{3/2}$ binding energy is shifted to a lower value for all the catalysts, conceivably indicating that the electron density of phosphorus increases after formation of the Co–P–B catalyst. In the case of the B 1s spectra (Fig. 6c), for all of the Co–P–B catalysts, the binding energy shift in the positive direction relative to the reported binding energy of elemental B (187.2 eV).[60] The

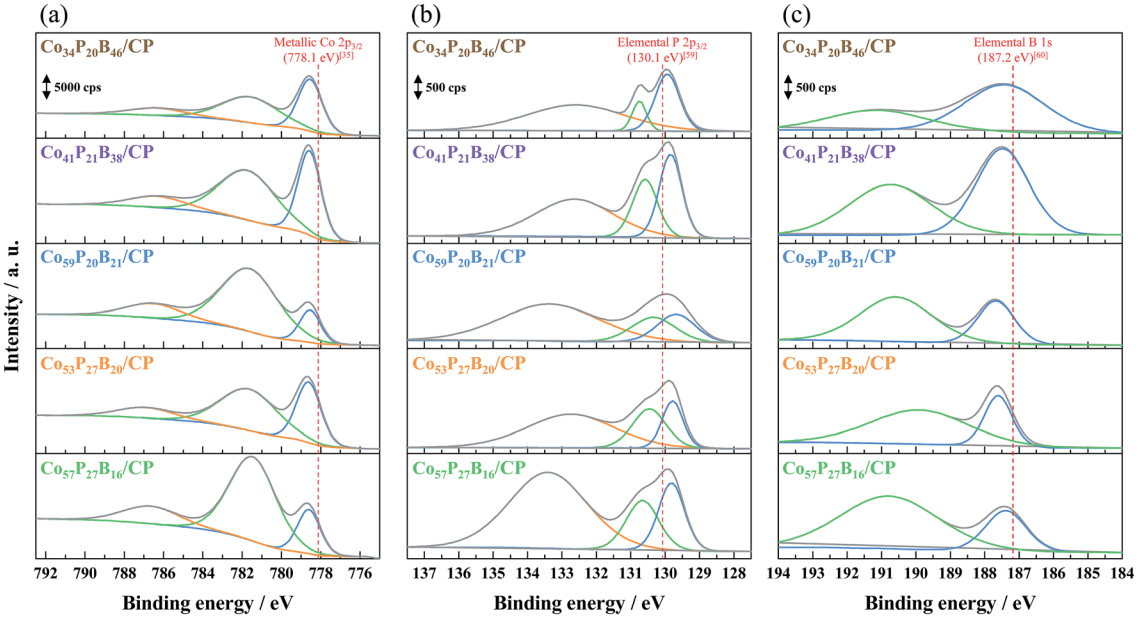


Fig. 6 XPS spectra of Co–P–B catalysts with various atomic composition: (a) Co 2p, (b) P 2p and (c) B 1s regions. Red dash line is binding energy of each elemental component.

Published on 21 February 2018. Downloaded by Chungang University on 4/17/2019 9:25:29 AM.

transferred electrons play a role in partially preventing the oxidation of cobalt.

The binding energies of the P $2p_{3/2}$ and B 1s peaks are summarized in Fig. 7a. The binding energy of P $2p_{3/2}$ is minimized (*i.e.*, showed the largest shift) when the B/P ratio in the catalysts is about 1 ($Co_{59}P_{20}B_{21}$/CP), whereas the binding energy of the B 1s peak shows the maximum value for the $Co_{59}P_{20}B_{21}$/CP catalyst. In the XPS spectra of reported Co–P catalysts, similar shifts of the binding energy to a higher value for Co 2p and a lower value for P 2p were observed for CoP_3 nanoneedles[36] and CoP nanowires,[39] owing to the difference in the electronegativity of Co and P. It should be noted that the shift in the binding energy was also influenced by the catalyst composition. In the case of the reported Co–B catalyst, electron transfer from B to Co occurred in the amorphous Co–B catalyst to fill the vacant d-orbital of cobalt,[49] making the Co in the Co–B catalyst electron-rich. Thus, it could be inferred that competitive electron transfer between Co–P and Co–B was operative in the electrodeposited Co–P–B catalysts and was maximized in the $Co_{59}P_{20}B_{21}$/CP catalyst having a B/P ratio of ~1. Similar results have been reported with Co–B–P[61] and Ni–P–B[62] prepared by a chemical reduction method for hydrogenation of ammonia borane and nitrobenzene, respectively. Furthermore, electron transfer between P and B is thought to have affected the binding energy shift. Because electron transfer is most effective between Co–P and Co–B,[63] the highest intrinsic activity was obtained with the $Co_{59}P_{20}B_{21}$/CP catalyst having a B/P ratio of ~1. As reported, the electron-rich P in the Co–P case[47] and the electron-rich Co in the Co–B case[60] provided active sites for the HER. Taking advantage of both effects, the synergetic effect between Co–P and Co–B in the $Co_{59}P_{20}B_{21}$/CP catalyst led to the highest intrinsic activity of this catalyst for the HER in the present study. When the B/P ratio was reduced to below ~1, the intrinsic HER activity of the catalysts gradually decreased. Compared to literature dealing with Co–P HER catalysts,[32,36,41,47,64–68] the $Co_{59}P_{20}B_{21}$/CP catalyst showed higher intrinsic activity, represented by the scaled current (Fig. 7b). Moreover, the $Co_{59}P_{20}B_{21}$/CP catalyst electrodeposited on CP is structurally advantageous for direct use as a cathode for PEMWE single cell operation.

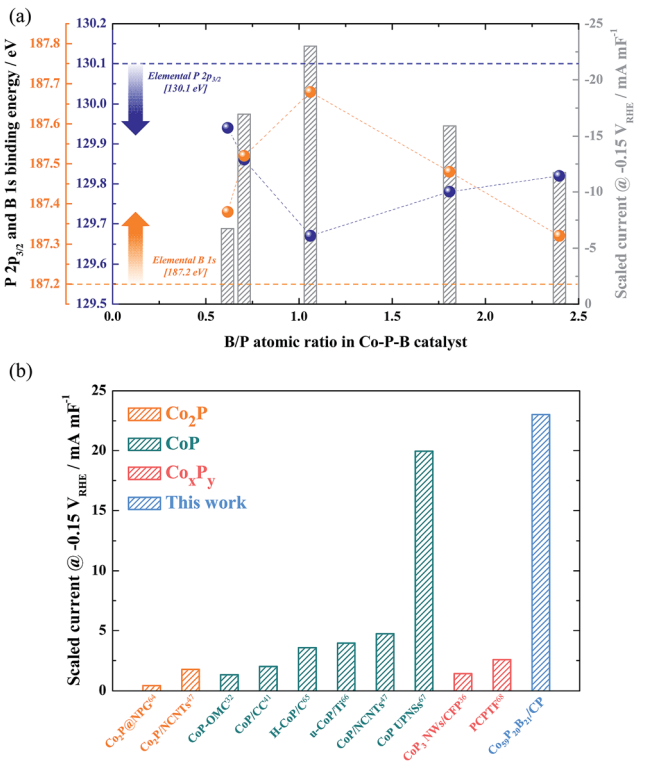


Fig. 7 (a) Scaled current of Co–P–B catalyst corresponding to binding energy of P $2p_{3/2}$ (navy) and B 1s (orange) with atomic ratio of catalyst. (b) Comparison of HER performance in 0.5 M H_2SO_4 with other CoP_x electrocatalysts reported in literature.[32,36,41,47,64–68]

Conclusions

Electrodeposition was used for the facile fabrication of Co–P–B catalysts on CP as a cathode for the PEMWE. By varying the electrolyte composition, the B/P ratio in the Co–P–B catalyst was easily controlled in the range of 0.61–2.39. Highly concentrated P and B sources in the deposition bath enabled the formation of an amorphous structure, thereby excluding the effect of the crystallinity on the HER activity. XPS analysis demonstrated that electron transfer from Co to P and from B to Co was operative among the three elements, depending on their relative ratios. The plot of the intrinsic activity for the HER as a function of the B/P ratio in Co–P–B catalysts showed volcano behaviour. The $Co_{59}P_{20}B_{21}$/CP catalyst having a B/P ratio of ~1 showed the highest HER intrinsic activity owing to the synergetic effect of electron transfer.

Conflicts of interest

There are no conflicts to declare.

Acknowledgements

This research was supported by the National Research Foundation of Korea (NRF) grant funded by the Korea government MSIT (2015R1C1A1A01055708 and 2016M3A7B4909369) and MOE (2016R1D1A1B03931963).

References

1 J. A. Turner, *Science*, 2004, **305**, 972–974.
2 A. Haryanto, S. Fernando, N. Murali and S. Adhikari, *Energy Fuels*, 2005, **19**, 2098–2106.
3 J. E. Funk, *Int. J. Hydrogen Energy*, 2001, **26**, 185–190.
4 K. Maeda, K. Teramura, D. Lu, T. Takata, N. Saito, Y. Inoue and K. Domen, *Nature*, 2006, **440**, 295.
5 P. C. Hallenbeck and J. R. Benemann, *Int. J. Hydrogen Energy*, 2002, **27**, 1185–1193.
6 M. Wang, Z. Wang, X. Gong and Z. Guo, *Renewable Sustainable Energy Rev.*, 2014, **29**, 573–588.
7 S. E. Hosseini and M. A. Wahid, *Renewable Sustainable Energy Rev.*, 2016, **57**, 850–866.
8 P. Dieguez, A. Ursua, P. Sanchis, C. Sopena, E. Guelbenzu and L. Gandia, *Int. J. Hydrogen Energy*, 2008, **33**, 7338–7354.

This journal is © The Royal Society of Chemistry 2018

Published on 21 February 2018. Downloaded by Chungang University on 4/17/2019 9:25:29 AM.

9 M. Carmo, D. L. Fritz, J. Mergel and D. Stolten, *Int. J. Hydrogen Energy*, 2013, **38**, 4901–4934.
10 K. Zeng and D. Zhang, *Prog. Energy Combust. Sci.*, 2010, **36**, 307–326.
11 C. C. Pavel, F. Cecconi, C. Emiliani, S. Santiccioli, A. Scaffidi, S. Catanorchi and M. Comotti, *Angew. Chem., Int. Ed. Engl.*, 2014, **53**, 1378–1381.
12 H. Kim, E. Hwang, H. Park, B.-S. Lee, J. H. Jang, H.-J. Kim, S. H. Ahn and S.-K. Kim, *Appl. Catal., B*, 2017, **206**, 608–616.
13 J. Wang, H. Zhu, D. Yu, J. Chen, J. Chen, M. Zhang, L. Wang and M. Du, *ACS Appl. Mater. Interfaces*, 2017, **9**, 19756–19765.
14 J. Chen, Y. Yang, J. Su, P. Jiang, G. Xia and Q. Chen, *ACS Appl. Mater. Interfaces*, 2017, **9**, 3596–3601.
15 E. J. Popczun, J. R. McKone, C. G. Read, A. J. Biacchi, A. M. Wiltrout, N. S. Lewis and R. E. Schaak, *J. Am. Chem. Soc.*, 2013, **135**, 9267–9270.
16 Y. Pan, Y. Liu, J. Zhao, K. Yang, J. Liang, D. Liu, W. Hu, D. Liu, Y. Liu and C. Liu, *J. Mater. Chem. A*, 2015, **3**, 1656–1665.
17 J. F. callejas, J. M. McEnaney, C. G. Read, J. C. Crompton, A. J. Biacchi, E. J. Popczun, T. R. Gordon, N. S. Lewis and R. E. Schaak, *ACS Nano*, 2014, **8**, 11101–11107.
18 J. F. Callejas, C. G. Read, C. W. Roske, N. S. Lewis and R. E. Schaak, *Chem. Mater.*, 2016, **28**, 6017–6044.
19 P. Xiao, M. A. Sk, L. Thia, X. Ge, R. J. Lim, J.-Y. Wang, K. H. Lim and X. Wang, *Energy Environ. Sci.*, 2014, **7**, 2624–2629.
20 P. Cao, J. Peng, J. Li and M. Zhai, *J. Power Sources*, 2017, **347**, 210–219.
21 Y. Sun, C. Liu, D. C. Grauer, J. Yano, J. R. Long, P. Yang and C. J. Chang, *J. Am. Chem. Soc.*, 2013, **135**, 17699–17702.
22 N. Kornienko, J. Resasco, N. Becknell, C. M. Jiang, Y. S. Liu, K. Nie, X. Sun, J. Guo, S. R. Leone and P. Yang, *J. Am. Chem. Soc.*, 2015, **137**, 7448–7455.
23 H. Li, P. Wen, Q. Li, C. Dun, J. Xing, C. Lu, S. Adhikari, L. Jiang, D. L. Carroll and S. M. Geyer, *Adv. Energy Mater.*, 2017, **7**, 1700513.
24 J. Masa, I. Sinev, H. Mistry, E. Ventosa, M. de la Mata, J. Arbiol, M. Muhler, B. Roldan Cuenya and W. Schuhmann, *Adv. Energy Mater.*, 2017, **7**, 1700381.
25 P. Zhang, M. Wang, Y. Yang, T. Yao, H. Han and L. Sun, *Nano Energy*, 2016, **19**, 98–107.
26 Z. Lv, M. Tahir, X. Lang, G. Yuan, L. Pan, X. Zhang and J.-J. Zou, *J. Mater. Chem. A*, 2017, **5**, 20932–20937.
27 H. W. Liang, S. Bruller, R. Dong, J. Zhang, X. Feng and K. Mullen, *Nat. Commun.*, 2015, **6**, 7992.
28 B. Cao, G. M. Veith, J. C. Neuefeind, R. R. Adzic and P. G. Khalifah, *J. Am. Chem. Soc.*, 2013, **135**, 19186–19192.
29 H. B. Wu, B. Y. Xia, L. Yu, X. Y. Yu and X. W. Lou, *Nat. Commun.*, 2015, **6**, 6512.
30 C. Wan, Y. N. Regmi and B. M. Leonard, *Angew. Chem., Int. Ed. Engl.*, 2014, **53**, 6407–6410.
31 W. F. Chen, J. T. Muckerman and E. Fujita, *Chem. Commun.*, 2013, **49**, 8896–8909.
32 M. Li, X. Liu, Y. Xiong, X. Bo, Y. Zhang, C. Han and L. Guo, *J. Mater. Chem. A*, 2015, **3**, 4255–4265.
33 L. Tian, X. Yan, X. Chen, L. Liu and X. Chen, *J. Mater. Chem. A*, 2016, **4**, 13011–13016.
34 E. J. Popczun, C. G. Read, C. W. Roske, N. S. Lewis and R. E. Schaak, *Angew. Chem., Int. Ed. Engl.*, 2014, **53**, 5427–5430.
35 M. Wei, L. Yang, L. Wang, T. Liu, C. Liu, Y. Tang and S. Luo, *Chem. Phys. Lett.*, 2017, **681**, 90–94.
36 T. Wu, M. Pi, D. Zhang and S. Chen, *J. Mater. Chem. A*, 2016, **4**, 14539–14544.
37 Z. Huang, Z. Chen, Z. Chen, C. Lv, M. G. Humphrey and C. Zhang, *Nano Energy*, 2014, **9**, 373–382.
38 J. Ryu, N. Jung, J. H. Jang, H.-J. Kim and S. J. Yoo, *ACS Catal.*, 2015, **5**, 4066–4074.
39 J. Tian, Q. Liu, A. M. Asiri and X. Sun, *J. Am. Chem. Soc.*, 2014, **136**, 7587–7590.
40 W. Gao, M. Yan, H.-Y. Cheung, Z. Xia, X. Zhou, Y. Qin, C.-Y. Wong, J. C. Ho, C.-R. Chang and Y. Qu, *Nano Energy*, 2017, **38**, 290–296.
41 X. Yang, A.-Y. Lu, Y. Zhu, M. N. Hedhili, S. Min, K.-W. Huang, Y. Han and L.-J. Li, *Nano Energy*, 2015, **15**, 634–641.
42 M. Liu and J. Li, *ACS Appl. Mater. Interfaces*, 2016, **8**, 2158–2165.
43 C. Wu, Y. Yang, D. Dong, Y. Zhang and J. Li, *Small*, 2017, **13**, 1602873.
44 N. Jiang, B. You, M. Sheng and Y. Sun, *Angew. Chem., Int. Ed. Engl.*, 2015, **54**, 6251–6254.
45 S. Oh, H. Kim, Y. Kwon, M. Kim, E. Cho and H. Kwon, *J. Mater. Chem. A*, 2016, **4**, 18272–18277.
46 D.-H. Ha, B. Han, M. Risch, L. Giordano, K. P. C. Yao, P. Karayaylali and Y. Shao-Horn, *Nano Energy*, 2016, **29**, 37–45.
47 Y. Pan, Y. Lin, Y. Chen, Y. Liu and C. Liu, *J. Mater. Chem. A*, 2016, **4**, 4745–4754.
48 G.-X. Cao, N. Xu, Z.-J. Chen, Q. Kang, H.-B. Dai and P. Wang, *ChemistrySelect*, 2017, **2**, 6187–6193.
49 S. Gupta, N. Patel, A. Miotello and D. C. Kothari, *J. Power Sources*, 2015, **279**, 620–625.
50 S. Gupta, N. Patel, R. Fernandes, R. Kadrekar, A. Dashora, A. K. Yadav, D. Bhattacharyya, S. N. Jha, A. Miotello and D. C. Kothari, *Appl. Catal., B*, 2016, **192**, 126–133.
51 P. Li, Z. Jin and D. Xiao, *J. Mater. Chem. A*, 2014, **2**, 18420–18427.
52 J. Delmas, L. Laversenne, I. Rougeaux, P. Capron, A. Garron, S. Bennici, D. Świerczyński and A. Auroux, *Int. J. Hydrogen Energy*, 2011, **36**, 2145–2153.
53 A. Martínez-Hernández, *Int. J. Electrochem. Sci.*, 2017, **12**, 1863–1873.
54 Y. N. Bekish, S. S. Grabchikov, L. S. Tsybul'skaya, V. A. Kukareko and S. S. Perevoznikov, *Prot. Met. Phys. Chem. Surf.*, 2013, **49**, 319–324.
55 L. Feng, H. Vrubel, M. Bensimon and X. Hu, *Phys. Chem. Chem. Phys.*, 2014, **16**, 5917–5921.
56 V. Vosoughi, S. Badoga, A. K. Dalai and N. Abatzoglou, *Ind. Eng. Chem. Res.*, 2016, **55**, 6049–6059.
57 F. H. Saadi, A. I. Carim, E. Verlage, J. C. Hemminger, N. S. Lewis and M. P. Soriaga, *J. Phys. Chem. C*, 2014, **118**, 29294–29300.

Published on 21 February 2018. Downloaded by Chungang University on 4/17/2019 9:25:29 AM.

58 C. G. Morales-Guio, L. A. Stern and X. Hu, *Chem. Soc. Rev.*, 2014, **43**, 6555–6569.
59 W. Cui, Q. Liu, Z. Xing, A. M. Asiri, K. A. Alamry and X. Sun, *Appl. Catal., B*, 2015, **164**, 144–150.
60 S. S. Muir, Z. Chen, B. J. Wood, L. Wang, G. Q. Lu and X. Yao, *Int. J. Hydrogen Energy*, 2014, **39**, 414–425.
61 Y. Men, J. Su, X. Du, L. Liang, G. Cheng and W. Luo, *J. Alloys Compd.*, 2018, **735**, 1271–1276.
62 S. P. Lee and Y. W. Chen, *J. Mol. Catal. A: Chem.*, 2000, **152**, 213–223.
63 N. Petal, R. Fernandes and A. Miotello, *J. Power Sources*, 2009, **188**, 411–420.
64 M. Zhuang, X. Ou, Y. Dou, L. Zhang, Q. Zhang, R. Wu, Y. Ding, M. Shao and Z. Luo, *Nano Lett.*, 2016, **16**, 4691–4698.
65 Y. Bai, L. Fang, H. Xu, X. Gu, H. Zhang and Y. Wang, *Small*, 2017, **13**, 1603718.
66 D. Zhou, L. He, W. Zhu, X. Hou, K. Wang, G. Du, C. Zheng, X. Sun and A. M. Asiri, *J. Mater. Chem. A*, 2016, **4**, 10114–10117.
67 C. Zhang, Y. Huang, Y. Yu, J. Zhang, S. Zhuo and B. Zhang, *Chem. Sci.*, 2017, **8**, 2769–2775.
68 Y. Yang, H. Fei, G. Ruan and J. M. Tour, *Adv. Mater.*, 2015, **27**, 3175–3180.

This journal is © The Royal Society of Chemistry 2018